Quantifying Low-keV Beam Damage in Ultrathin MFI Zeolite Nanosheets with an SEM

Jason Holm
Applied Chemicals and Materials Division
Materials Measurement Laboratory
National Institute of Standards and Technology (NIST)
325 Broadway, MS 647
Boulder, CO 80305.

Abstract

This manuscript demonstrates the susceptibility of ultrathin Mobil Five (MFI) zeolite nanosheets to low-keV electron beam damage in a scanning electron microscope (SEM). Beam dose rates and characteristic beam doses are quantified at beam energies from 15 keV to 30 keV using an on-axis transmission electron detector to measure signal decay times in diffraction patterns and by underfocusing to enable spot size measurement. Characteristic beam doses ranged from approximately 1.9 C/cm^2 at 15 keV to 14 C/cm^2 at 30 keV, and the damage mechanism was attributable to radiolysis but other processes including electrostatic charging and sputtering could not be ruled out.

keywords: beam damage, dose, dose rate, SEM, , STEM-in-SEM, zeolite, 2D materials

Introduction

The last decade has seen a resurgence in transmission imaging and diffraction methods in the scanning electron microscope (SEM) (Keller et al., 2022). One reason for this is the relatively recent, increasing implementation of electron detectors that enable low energy transmission electron imaging and diffraction with beam energies ranging from approximately 3 keV to 30 keV (Klein et al., 2012; Brodu et al., 2017; Caplins et al., 2019; Orekhov et al., 2020). Another reason is the emergence of new materials that lend themselves to the low beam energies typical of conventional SEMs. Two-dimensional (2D) materials and low-Z materials immediately come to mind as ostensibly ideal candidates for scanning transmission electron microscopy in a scanning electron microscope (STEM-in-SEM). The inherently thin dimension of 2D materials is generally on the same order of magnitude as the electron mean free path at SEM energies, meaning that image interpretation is not overly complicated because of multiple scattering events, and low-Z materials may benefit from the larger characteristic scattering angles of electrons in the SEM compared to higher energy electron microscopes. For example, the larger scattering angles can give rise to stronger contrast that can be beneficial for observing small changes in mass-thickness commonly found in biomaterials and other organic materials (Kuwajima et al., 2013).

While some materials in those broad classes may be ideal for low-energy transmission electron studies, many are also susceptible to electron beam damage. For example, as a material class zeolites are especially beam sensitive and avoiding damage is a significant challenge regardless of the electron beam energy (Csencsits and Gronsky, 1987; Pan and Crozier, 1993; Ugurlu et al., 2011; Cretu et al., 2015). Even in the SEM, the crystalline structure degrades

extremely rapidly with electron beam exposure, and mass displacement is evident at beam energies as low as 15 keV (vide infra).

Beam damage mechanisms include displacement damage (knock-on and sputtering), ionization damage (radiolysis), electrostatic charging, and heating. Several recent articles provide an excellent overview of damage mechanisms in different materials and also point to the importance of quantifying and minimizing damage (Jiang, 2016; Egerton, 2019; Chen et al., 2020; Ilett et al., 2020). The predominant damage mechanism can depend on different parameters including material type (i.e., insulator, conductor, organic, inorganic), sample geometry (i.e., solid, porous, bulk, 2D, etc.), and beam energy. For example, knock-on damage may not be prevalent at conventional SEM energies for inorganic conducting samples, but there is no practical lower energy threshold for organic samples to avoid ionization damage (Egerton, 2012; Egerton, 2019). As the electron beam energy E_0 is reduced, the inelastic scattering cross-section increases approximately as $1/E_0$ and therefore the ionization damage sensitivity increases. Although electron scattering physics is well understood, commonly applied theories cannot always explain the observed damage behavior, particularly at typical SEM energies (Gu et al., 2017), and multiple damage mechanisms may also be simultaneously active in some samples depending on the beam energy (Ugurlu et al., 2011).

Beam damage can be quantified in terms of particle fluence, defined as the number of primary electrons incident per unit area of sample ($e^-/Å^2$) (Egerton, 2019). The concept of a characteristic or critical dose is often invoked when quantifying beam damage (Egerton et al., 2004). The characteristic dose can be defined different ways, but here it is defined as the fluence at which the intensity of a particular reflection in an electron diffraction spot pattern decreases to $1/e$ of the initial intensity, or $I/I_0 \approx 0.368$. Quantifying beam dose, in general, is not

straightforward in an SEM because the direct beam spot size at optimal focus conditions is too small to easily measure, particularly with modern field emission SEMs (FE-SEMs). Moreover, for thicker samples where damage zones extend beyond the direct beam into a teardrop-shaped interaction volume, it becomes especially difficult to quantify the spatial extent of the damage zone and hence obtain a characteristic dose. Using an ultrathin sample can perhaps alleviate that issue. Furthermore, on-axis diffraction cameras that enable fast diffraction pattern intensity decay rates to be used as a damage metric have not seen use in SEMs until very recently. To those ends, previous SEM beam damage studies have employed conventional transmission electron microscopy (TEM) to measure damage zones (Howie et al., 1986; Gu et al., 2017). Electron energy loss spectroscopy has also been used to assess beam damage (Isaacson et al., 1973; Egerton et al., 2006; Ugurlu et al., 2011), but those accessories are extremely rare on SEMs.

For these and other reasons, characteristic beam dose assessments have not been as widely pursued in the SEM as they have in higher energy electron microscopes. However, the resurgence in transmission electron techniques in an SEM has brought with it the incorporation of on-axis diffraction detectors that can, in some instances, enable beam damage to be quantified without resorting to other characterization tools. To that end, this manuscript demonstrates the extreme susceptibility of 2D MFI zeolite nanosheets to low-keV electron beam damage in a conventional SEM by measuring diffraction pattern (DP) intensity decay rates and the spatial extent of the damage zone. Dose, dose rate, and characteristic dose are quantified at beam energies from 15 keV to 30 keV.

Experimental

A Zeiss* Sigma 300 VP SEM was used for all imaging and diffraction. Figure 1a shows a representative image of several overlapping 2D MFI zeolite nanosheets recorded using the InLens secondary electron detector, 20 keV primary electrons, and a 30 μm aperture (beam current ≈ 440 pA). The sheets are nominally two unit cells thick (i.e., approximately 5 nm thick) and supported on an ultrathin carbon/lacey carbon substrate (Jeon, et al., 2017). Smaller bright seed crystals and wrinkling can be observed in the image. Real space transmission images were recorded with the Zeiss aSTEM solid-state detector, and diffraction pattern videos were recorded with a retractable scintillator-coupled digital camera. Figure 1b shows the experimental setup of the retractable scintillator-coupled camera. Here, a YAG:Cd scintillator and a Thorlabs 340M camera were used. A complete description of the detector can be found elsewhere (Caplins et al., 2020). For all experiments, the sample was positioned between the SEM pole piece and scintillator using a cantilevered, three-slot sample holder (Fig. 1c).

Two slightly different approaches were used to quantify beam damage parameters. Neither was designed to minimize beam damage. In the first approach, the intent was to obtain $t_{1/e}$ decay times of the (200) reflection as a function of primary electron energy with the beam focused to obtain the smallest spot size at the sample. With the sample held stationary at approximately 13.78 mm working distance (WD), the electron beam was manually positioned at several locations on the sample and the digital camera was used to record videos of fading DPs at beam energies ranging from 15 keV to 30 keV. To ensure that the signal was obtained from regions of the sample comprising only single sheet thickness, a fast-scan low pixel density secondary electron image was recorded prior to recording the videos and used as a guide to manually position the electron beam.

In the second approach, the primary electron beam was focused at different WDs ranging from at the sample (13.78 mm) to 100 μm *below* the sample (13.88 mm) to obtain different primary electron beam spot sizes. For example, at each energy the beam was first focused at the sample WD and a video was recorded of fading DPs at different locations on the sample. Without moving the sample along the optic axis or changing the electron accelerating voltage, underfocus was then implemented by typing the desired WD into the SEM control software. At each combination of beam energy and underfocus, the beam was positioned manually and held stationary at several locations while a video of the fading DP was recorded at each location. For both approaches, videos were recorded using a 500 Hz frame rate, 1 pixel × 1 pixel binning, and a 100 pixel × 100 pixel sensor area. A 30 μm aperture was used to limit the beam current (measured using a Faraday cup) from approximately 515 pA (15 keV) to 660 pA (30 keV). From the videos recorded using both approaches, the average intensity of the (200) reflection was quantified as a function of time, and an exponential decay function was fit to the data to determine the time, $t_{1/e}$, required for the average intensity to decrease to $1/e$ of the initial intensity. MATLAB* was used for video and data processing.

Results

Figure 2a shows traces of the average video frame intensity as a function of time for beam energies ranging from 15 keV to 30 keV. Here, the beam was specifically focused at the sample (i.e., WD ≈ 13.78 mm). Sharp peaks in the different traces correspond to each time the beam was repositioned on the sample, and the signal decay is representative of how the *entire* DP fades with beam exposure. For example, each point in the different traces represents the average intensity of a single 100 pixel × 100 pixel video frame which encompassed several orders of diffraction spots including the direct beam. A representative video frame from one of

the peak locations the 30 keV video dataset is shown inset in the figure, and the (200) reflection is indicated by the inset arrow. Beam dwell time at each manually selected position was approximately 5 seconds. Notice that as the beam energy was reduced the sharp peaks that occurred each time the beam was repositioned also decreased in intensity. This was due to a combination of factors including the decreasing beam current as the accelerating voltage was reduced and the conversion efficiency of the scintillator, which decreases with incident electron energy.

The sharp peak positions in Fig. 2a were used as a starting point from which the average intensity of the background-subtracted (200) reflection was quantified as a function of time. Although numerous peaks appear in the traces of Figure 2a, DPs were only used if there was no strong evidence of sample wrinkling (Kumar et al., 2015) or significant deviation from the [010] zone axis. Figure 2b shows representative traces of the intensity of the background-subtracted (200) reflection as a function of time at each beam energy. The inset of Figure 2b summarizes the average $t_{1/e}$ decay times when focus was at the sample WD. Regardless of beam energy, $t_{1/e}$ was approximately 40 ms. Practically speaking, for 5 nm thick MFI nanosheets supported on an ultrathin carbon substrate, several tens of milliseconds is a reasonable upper time limit for collecting single DPs under the conditions used here (i.e., with focus at the sample) without incurring significant signal degradation due to increasing sample damage.

One way to extend $t_{1/e}$ is by underfocusing the primary electron beam, thereby effectively distributing the beam current over a larger area of the sample. (Underfocus is defined here as setting the WD below the sample, or further away from the objective lens.) Although the point-to-point spatial resolution for conventional SEM imaging is not optimal when using this approach, the benefit is that the diffraction signal collection time can be significantly extended,

which can result in a stronger signal-to-noise ratio over a wider range of operating conditions. More importantly, by underfocusing, the increased spot size at the sample also allows the damage zone diameter to be measured in a straightforward manner and a characteristic beam dose to be determined. For example, Figure 3 shows representative images of the sample after a 30 keV beam was manually positioned at different locations with focus at the sample (WD ≈ 13.78 mm, Fig. 3a), 10 μm under the sample (WD ≈13.79 mm, Fig. 3b), 20 μm under the sample (WD ≈ 13.80 mm, Fig. 3c), and 50 μm under the sample (WD ≈ 13.83 mm, Fig. 3d). The inset arrows point to dark spots that are suggestive of damage where the beam was positioned.

At the smallest spot sizes the image contrast at the specified positions is indicative of through-holes in the zeolite nanosheets (Fig. 3a, Fig. 3b). Although not shown here, similar contrast was observed when 15 keV electrons were used. This is somewhat surprising given that the sample is supported on an ultrathin carbon substrate which is thought to help minimize displacement-type damage (Egerton, 2010; Zan et al., 2013). Moreover, the faint brighter halos around the spots in Fig. 3c and Fig. 3d are suggestive of sample sputtering or perhaps charging (Downing et al. 2004). To that end, transmission electron images were recorded in the SEM to support the conjecture that the spots are holes rather than other imaging artifacts such as beam-induced contamination. Figure 4a shows a secondary electron image of the sample with damage spots obtained using three underfocus settings. The smallest spots on the far-right side of the image appear to be through-holes even at positions where two zeolite nanosheets overlap (indicated by the thicker red arrows). In the bright-field transmission image (Fig. 4b) the spots are brighter than the surrounding areas, and in the annular dark-field transmission image (Fig. 4c) the spots are darker than the surrounding region. In all three images, the contrast of the indicated spots compared to the immediately surrounding areas is a strong indication that the

sample is damaged, and that material displacement is likely as a result of beam-sample interaction.

To quantify characteristic beam dose, the cross-sectional area of the primary electron beam at the sample must be known. To that end, the diameters of damage zones like those in Figure 3 and Figure 4 were measured as a function of underfocus and taken as a surrogate for the diameter of the primary electron beam. (Using the damage zone as beam diameter surrogate is not unreasonable because when astigmatism is intentionally added to the to the primary electron beam, the non-circular shape is also evident in the damage zone. For example, see Fig. 3e.) As Figure 5a shows, the damage zone diameter increases approximately linearly with increasing underfocus. This is not surprising since the variation in underfocus is small compared to the sample WD (i.e., the sample was at 13.78 mm and the maximum underfocus was 100 μm, or WD = 13.88 mm). Note that when the beam is focused between the sample and approximately 10 μm under the sample, measurements of the damage zone may not be truly representative of the actual beam spot size because obtaining focus exactly at the sample plane can be challenging even in ideal environment. The WD of a well-focused image can also vary depending on the accelerating voltage. For these and other reasons, including the fact that through-holes were created in the sample, dose calculations at focus and at the smallest underfocus settings should be interpreted with caution.

Taken together with electron beam current measured using a Faraday cup, the average damage zone diameters (Fig. 5a) and the $t_{1/e}$ decay times obtained from video data of fading DPs (Fig. 5b) can be used to calculate the beam dose rate ($e^-/(Å^2 s)$, Fig. 5c) and dose at $t_{1/e}$ ($e^-/Å^2$, Fig. 5d) for different beam energies. As Figure 5b shows, $t_{1/e}$ increases approximately quadratically with underfocus. This trend is reasonable given that the beam current is unchanged at a chosen

beam energy, but the effective area over which it is spread increases with the square of the damage zone diameter. As Figure 5d shows, when the underfocus is greater than approximately 20 μm (i.e., the beam is spread to a diameter that does not produce through-holes at the timescales employed here), the dose approaches an approximately constant value that depends on beam energy. These constant values, calculated as the average dose from 20 μm to 100 μm underfocus, are shown in the inset table and are interpreted as the characteristic dose for the sample under the specified operating conditions. Notably, the characteristic dose decreases with decreasing beam energy, meaning that as the beam energy is reduced it takes fewer electrons to impart the same amount of damage as is done at higher beam energies.

Discussion

MFI zeolite DP intensity decay rates and characteristic doses have been examined previously, albeit at significantly greater beam energies. For example, in one report employing 400 keV electrons, a 2 Å dose-limited resolution was established by noting the disappearance of the (10 0 0) reflection at a dose of approximately 300 $e^-/Å^2$ (Pan and Crozier, 1993). Based on the order of magnitude difference in beam energies and the difference in sample configuration (i.e., they examined powder), it is difficult to make a direct comparison with the results presented here. Although the (10 0 0) reflection can be observed using the SEM at 15 keV with focus at the sample, the 500 Hz frame rate required to capture the decay of the (200) reflection with sufficient temporal resolution was too fast to allow observation of weaker high order reflections. It is also difficult to make a direct comparison of the characteristic dose for the (10 0 0) and (200) reflections because higher order reflections are more sensitive to structural changes and will lose intensity more rapidly than reflections closer to the direct beam. However, the damage mechanism in that report was attributed to radiolysis by another author (Egerton, 2012), which is

in line with the results obtained here (vide infra). Elsewhere, 300 keV electrons were used to examine 2D MFI nanosheets practically identical to the ones examined here (Kumar, 2015). Although the (200) reflection was not specifically studied, the decay times of other low order reflections were several orders of magnitude longer than those reported here. For example, the intensity of the (303) reflection did not decay by more than 40% even after 100 minutes. It is noteworthy that by decreasing the beam energy one order of magnitude from 300 keV to 30 keV, $t_{1/e}$ decreases by several orders of magnitude. Naturally then, one might ask what happens when the beam energy is reduced an additional order of magnitude from 30 keV to 3 keV. Does $t_{1/e}$ decrease again by several orders of magnitude? Does a lower cutoff energy exist at which damage is no longer an issue, and is that lower energy practical for imaging and analytical purposes? The scintillator-coupled camera used here is not effective 3 keV, and although direct electron detection cameras that can record 3 keV signals have seen use in SEMs (Orekhov et al., 2020), the maximum frame rate of those devices (40 Hz) is not sufficiently fast to capture the DP decay rate for this material at the beam energies used here. Significantly faster direct electron detection cameras are commercially available (MacLaren et al., 2020), but they are largely dedicated to higher energy electron detection and not yet optimized or commercially available for low keV SEM applications.

Regarding the damage mechanism responsible for the holes observed in the nanosheet sample, some speculation is offered. There are very few reports on beam damage at conventional SEM energies, but general guidelines to distinguish between sputtering and radiolysis have been given for inorganic samples at beam energies between 100 keV and 300 keV (Egerton, 2012). For example, one guideline suggests that for radiolysis the characteristic dose increases with increasing beam energy. As the inset table of Figure 5d shows, the

characteristic dose increases approximately linearly with beam energy so one could infer that radiolysis is an active damage mechanism. Another guideline is that a characteristic dose < 1000 C/cm^2 points to radiolysis. The characteristic doses tabulated in Figure 5 are well below this threshold. If these two guidelines are assumed to be valid at lower beam energies, then the damage mechanism can be tentatively assigned to radiolysis.

Although radiolysis involves bond breakage and structural degradation which could lead to the appearance of holes, other mechanisms could be occurring simultaneously and should be considered. For example, conventional knowledge suggests that sputtering is unlikely at SEM beam energies (Egerton et al., 2010). However, the zeolite nanosheet examined here is both porous *and* 2D meaning that the surface area-to-volume ratio is very large. Because the binding energy for surface atoms and displacement energy for atoms adjacent to pores is lower than it is for atoms in the bulk, sputtering should not be overlooked as a damage mechanism. To that end, the faint bright halos around the damaged areas in the secondary electron images of Figure 3d and Figure 4a are suggestive of sputtered material redeposited around the perimeter of the holes. However, transmission images, which can reveal small changes in mass-thickness (Holm et al., 2020), do not show contrast indicative of redeposited material. Alternatively, the halos could be an artifact of electrostatic charging which can induce displacement damage (Egerton, 2019). Electrostatic charging is generally much more apparent in secondary electron (SE) images than in transmission images in the SEM, and this behavior was observed while imaging the sample using secondary electrons. For example, Figure 6 shows a conventional SE image recorded using the InLens detector after the sample was intentionally damaged with a 15 keV electron beam positioned at different locations. Two bright horizontal lines, a strong indication of sample charging, can be observed extending from one of the damage spots. These lines do not always

appear at every damage spot, but they only appear after the sample has been previously subjected to intentional beam damage. Moreover, in regions where the ultrathin carbon support film is missing and the zeolite nanosheets are only supported by lacey carbon, sample charging is also apparent at the edges of the nanosheets in transmission images. To that end, an internal electric field induced by the electron beam may be partially responsible for specimen thinning and/or hole formation due to ion migration or dielectric breakdown (Egerton, 2012). In another report, Gu et al. (2017) reported sputtering damage, restructuring, and formation and amorphization of precipitates in a Zircaloy-4 sample at 30 keV in an FE-SEM. This result is notable because the sputtering threshold for Zr atoms (210 keV) is significantly higher than 30 keV. The observations were tentatively attributed to the high beam current density (on the order of A/cm^2, which is comparable to what was used in this work) and the relatively high energy deposition rate. When the electron beam is optimally focused at the sample WD, the beam spot size is of similar dimension to the MFI zeolite unit cell (i.e, lattice parameters $a \approx b \approx 2$ nm, $c \approx 1.3$ nm) (Olson et al., 1981). Therefore, the entire beam current is incident on a relatively small number of bonds and a dose rate effect may be possible. Dose rate effects could conceivably be investigated by using the SEM extractor voltage to vary the beam current. Although it is beyond the scope of this contribution to definitively identify the exact damage mechanism(s), anecdotal evidence suggests that radiolytic damage is likely, and that sample charging and sputtering may also play a role in producing holes in the sample.

Conclusions

MFI zeolites are susceptible to beam damage even at conventional SEM energies. This damage can be quantified in a straightforward manner in the SEM using a moderately fast diffraction camera to measure the decay rate of the intensity in the (200) reflection. Under

normal SEM operating conditions (i.e., with focus at the sample), $t_{1/e}$ was approximately 40 milliseconds for beam energies between 15 keV and 30 keV and through-holes appeared wherever the beam was positioned on the sample for longer times. By underfocusing, or spreading the beam, through holes could be avoided but damage was still apparent. By measuring the size of the damage zone, it was possible to quantify a characteristic dose at different beam energies and show that the sample was more susceptible to beam damage as the primary electron energy was reduced from 30 keV to 15 keV. The approach used here (i.e., underfocusing the beam to disperse the current over a larger sample area) could be useful to assess beam damage in other material systems. Although there will always be challenges to obtaining high-resolution real-space STEM-in-SEM images from samples that are ultrasensitive to beam damage, knowing the limitations of the sample under different illumination conditions is key to efficiently obtaining information.

References

* Certain commercial products or company names are identified to adequately describe the study. Such identification does not imply recommendation or endorsement by the National Institute of Standards and Technology, nor does it imply that the products are necessarily the best available for the purpose.

Brodu, E., Bouzy, E., & Fundenberger, J. (2017). On-axis transmission Kikuchi diffraction for orientation mapping of nanocrystalline materials in the SEM. *Microscopy and Microanalysis* **23**(S1), 530-531. https://doi.org/10.1017/S1431927617003336.

Caplins, B.W., Holm, J.D., Keller, R.R. (2019). Transmission imaging with a programmable detector in a scanning electron microscope. *Ultramicroscopy* **196**, 40-48. https://doi.org/10.1016/j.ultramic.2018.09.006.

Caplins, B.W., Holm, J.D., White, R.M. & Keller, R.R. (2020). Orientation mapping of graphene using 4D STEM-in-SEM. *Ultramicroscopy* **219**, 113137. https://doi.org/10.1016/j.ultramic.2020.113137.

Chen, Q., Dwyer, C., Sheng, G., Zhu, C., Li, X., Zheng, C. & Zhu, Y. (2020). Imaging beam-sensitive materials by electron microscopy. *Adv. Mater.* **32**, 1907619. https://doi.org/10.1002/adma.201907619.

Cretu, O., Lin, Y.C. & Suenaga, K. (2015). Inelastic electron irradiation damage in hexagonal boron nitride. *Micron* **72**, 21-27. https://doi.org/10.1016/j.micron.2015.02.002.

Csencsits, R. & Gronsky, R. (1987). Damage of zeolite Y in the TEM and its effects on TEM images. *Ultramicroscopy* **23**, 421-431. https://doi.org/10.1016/0304-3991(87)90253-1.

Downing, K., McCartney, M., & Glaeser, R. (2004). Experimental Characterization and Mitigation of Specimen Charging on Thin Films with One Conducting Layer. *Microscopy and Microanalysis* **10**(6), 783-789. https://doi.org/10.1017/S143192760404067X.

Egerton, R. (2012), Mechanisms of radiation damage in beam-sensitive specimens, for TEM accelerating voltages between 10 and 300 kV. *Microsc. Res. Tech.* **75,** 1550-1556. https://doi.org/10.1002/jemt.22099.

Egerton, R.F. (2019). Radiation damage to organic and inorganic specimens in the TEM. *Micron* **119**, 72-87. https://doi.org/10.1016/j.micron.2019.01.005.

Egerton, R. F., Li, P. & Malac. M. (2004). Radiation damage in the TEM and SEM. *Micron* **35**, 399-409. https://doi.org/10.1016/j.micron.2004.02.003.

Egerton, R.F., McLeod, R., Wang, F. & Malac, M. (2010). Basic questions related to electron-induced sputtering in the TEM. *Ultramicroscopy* **110**(8), 991-997. https://doi.org/10.1016/j.ultramic.2009.11.003.

Egerton, R.F., Wang, F. & Crozier, P.A. (2006). Beam-induced damage to thin specimens in an intense electron probe. *Microsc. Microanal.* **12**(1), 65-71. https://doi.org/10.1017/S1431927606060065.

Gu, H., Li, G., Liu, C., Yuan, F., Han, F., Zhang, L., Wu, S. (2017). Considerable knock-on displacement of metal atoms under a low energy electron beam. *Sci. Rep.* **7**, 184. https://doi.org/10.1038/s41598-017-00251-3.

Holm, J., Caplins, B. & Killgore, J. (2020). Obtaining diffraction patterns from annular dark-field STEM-in-SEM images: Towards a better understanding of image contrast. *Ultramicroscopy* **212**, 112972. https://doi.org/10.1016/j.ultramic.2020.112972.

Howie, A., Rocca, F. J. & Valdrè, U. (1985). Electron beam ionization damage processes in p-terphenyl. *Philosophical Magazine B* **52**, 751-757. https://doi.org/10.1080/13642818508240634.

Ilett, M., S'ari, M., Freeman, H., Aslam, Z., Koniuch, N., Afzali, M., Cattle, J., Hooley, R., Roncal-Herrero, T., Collins, S. M., Hondow, N., Brown, A., & Brydson, R. (2020). Analysis of complex, beam-sensitive materials by transmission electron microscopy and associated techniques. *Philosophical transactions. Series A, Mathematical, physical, and engineering sciences* **378**(2186), 20190601. https://doi.org/10.1098/rsta.2019.0601.

Isaacson, M., Johnson, D. & Crewe A.V. (1973). Electron beam excitation and damage of biological molecules; Its implications for specimen damage in electron microscopy. *Radiat. Res.* **55**(2), 205–224. https://doi.org/10.2307/3573678.

Jeon, M.Y., Kim, D., Kumar, P., Lee, P.S., Rangnekar, N,. Bai, P., Shete, M., Elyassi, B., Lee, H.S,. Narasimharao, K., Basahel, S.N., Al-Thabaiti, S., Xu, W., Cho, H.J., Fetisov, E.O., Thyagarajan, R., DeJaco, R.F., Fan, W., Mkhoyan, K.A., Siepmann, J.I. & Tsapatsis, M. (2017). Ultra-selective high-flux membranes from directly synthesized zeolite nanosheets. *Nature* **543**(7647), 690-694. https://doi.org/10.1038/nature21421.

Jiang N. (2013). Damage mechanisms in electron microscopy of insulating materials. *J. Phys. D: Appl. Phys.* **46**, 305502. https://doi.org/10.1088/0022-3727/46/30/305502.

Jiang N. (2016). Beam damage by the induced electric field in transmission electron microscopy. *Micron* **83**, 79-92. https://doi.org/10.1016/j.micron.2016.02.007.

Keller, R. R., Caplins, B. W. & Holm, J. D. (2022). STEM-in-SEM: A re-emerging material measurement approach, *Microscopy and Analysis* **60**, 14-17.

Klein, T., Buhr, E., Frase, C. G. (2012). TSEM: A Review of Scanning Electron Microscopy in Transmission Mode and Its Applications. Advances in Imaging and Electron Physics, Vol. 171, 297-356. https://doi.org/10.1016/B978-0-12-394297-5.00006-4.

Kumar, P., Agrawal, K., Tsapatsis, M. & Mkhoyan, A. K. (2015). Quantification of thickness and wrinkling of exfoliated two-dimensional zeolite nanosheets. *Nat. Commun.* **6**, 7128. https://doi.org/10.1038/ncomms8128.

Kuwajima, M., Mendenhall, .J.M, Lindsey, L.F., Harris, K.M. (2013). Automated transmission-mode scanning electron microscopy (tSEM) for large volume analysis at nanoscale resolution. *PLoS ONE 8*(3): e59573. https://doi.org/10.1371/journal.pone.0059573.

MacLaren, I., Macgregor, T. A., Allen, C.S., and Kirkland, A. I. (2020). Detectors—The ongoing revolution in scanning transmission electron microscopy and why this important to material characterization. *APL Materials* **8**, 110901. https://doi.org/10.1063/5.0026992.

Olson, D.H., Kokotailo, G.T., Lawton, S.L. & Meier W.M. (1981). Crystal structure and structure-related properties of ZSM-5. *J. Phys. Chem.* **85**, 2238-2243. https://doi.org/10.1021/j150615a020.

Orekhov, A., Jannis, D., Gauquelin, N., Guzzinati, G., Nalin Mehta, A., Psilodimitrakopoulos, S., Mouchliadis, L., Sahoo, P. K., Paradisanos, I., Ferrari, A.C., Kioseoglou, G., Stratakis, E. & Verbeeck, J. (2020). Wide field of view crystal orientation mapping of layered materials. arXiv preprint. https://doi.org/10.48550/arXiv.2011.01875.

Pan, M., (1996). High resolution electron microscopy of zeolites. *Micron* **27**(3-4) 219-238. https://doi.org/10.1016/0968-4328(96)84210-7.

Pan, M. & Crozier, P.A. (1993). Low-dose high-resolution electron microscopy of zeolite materials with a slow-scan CCD camera. *Ultramicroscopy* **48**, 332-340. https://doi.org/10.1016/0304-3991(93)90108-A.

Ugurlu, O., Haus, J., Gunawan, A. A., Thomas, M. G., Maheshwari, S., Tsapatsis, M. & Mkhoyan, K. A. (2011). Radiolysis to knock-on damage transition in zeolites under electron beam irradiation. *Phys. Rev. B* **83**, 113408. https://doi.org/10.1103/PhysRevB.83.113408.

Zan, R., Ramasse, Q. M., Jalil, R., Georgiou, T., Bangert, U. & Novoselov, K.S. (2013). Control of Radiation Damage in MoS2 by Graphene Encapsulation. *ACS Nano* **7** (11), 10167-10174. https://doi.org/10.1021/nn4044035.

Figures

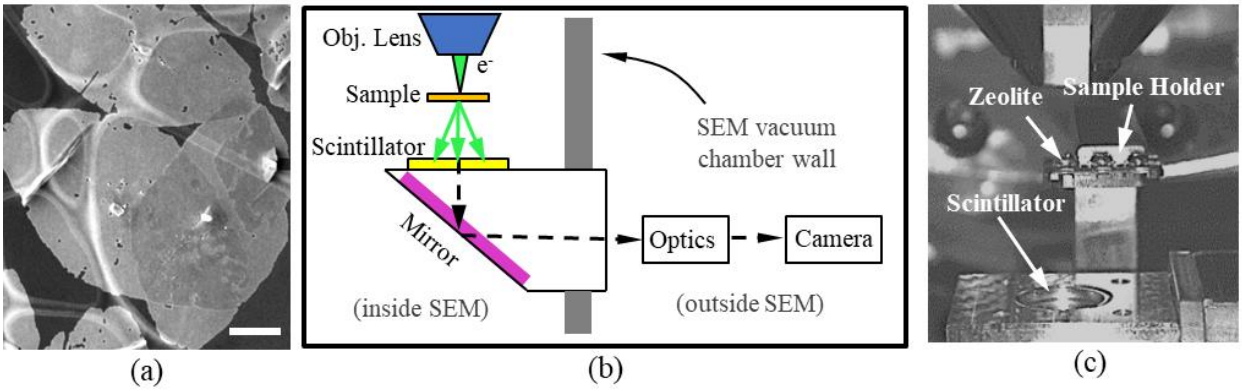

Figure 1. (a) A secondary electron image of 2D MFI nanosheets supported on an ultrathin carbon substrate recorded using the InLens detector, 20 keV primary electrons and WD = 13.78 mm. Scale bar is 400 nm. (b) A schematic of the experimental setup for recording DP videos. (c) An image of the SEM chamber interior showing the sample position and some detector hardware.

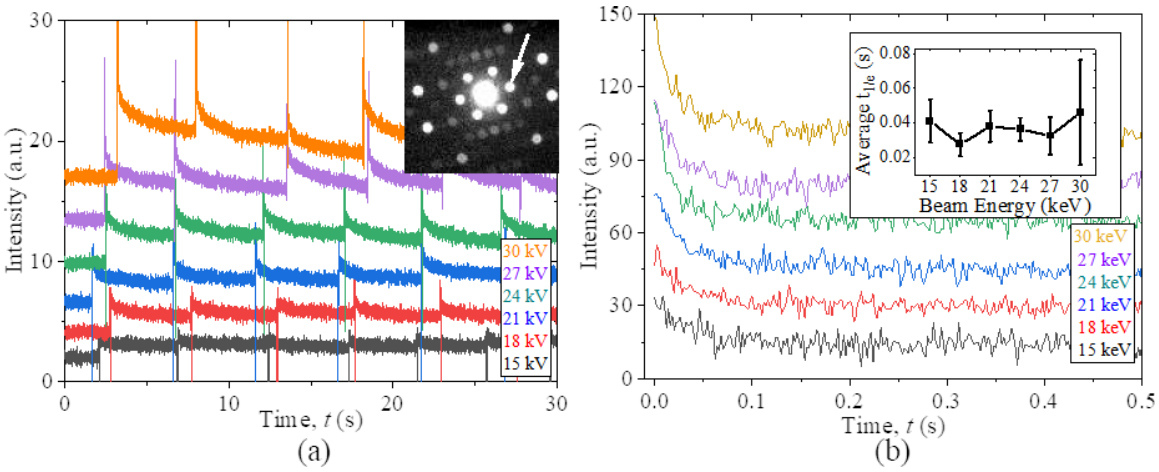

Figure 2. DP intensities as a function of time at different beam energies with focus at the sample. (a) Traces of the average video frame intensity. The inset DP shows a single unmodified frame from a 30 keV video. The (200) reflection is indicated. (b) Representative intensity traces of the background-subtracted (200) reflection shifted to t = 0 s for comparison. The inset plot summarizes the average $t_{1/e}$ decay times at different beam energies. Error bars represent standard deviation.

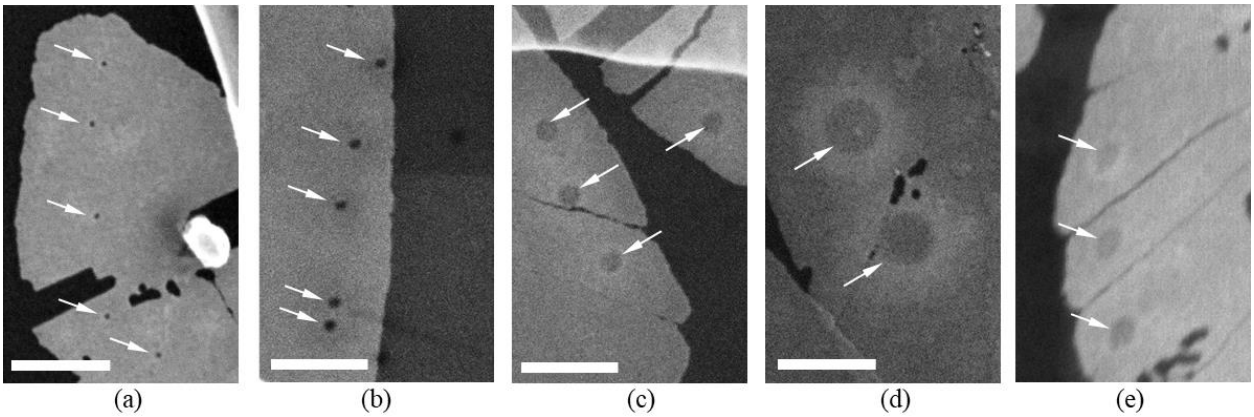

Figure 3. Secondary electron images of zeolite nanosheets after probing the sample at different manually selected positions with a 30 keV beam focused at different WDs. (a) WD = 13.78 mm (focus at the sample). (b) WD = 13.79 mm (focus 10 μm under the sample). (c) WD = 13.80 mm (focus 20 μm under the sample). (d) WD = 13.83 mm (focus 50 μm under the sample). (e) Damage zones created with astigmatism intentionally added to a 15 keV primary electron beam and 20 μm underfocus. Inset arrows indicate beam positions. Scale bars are 200 nm.

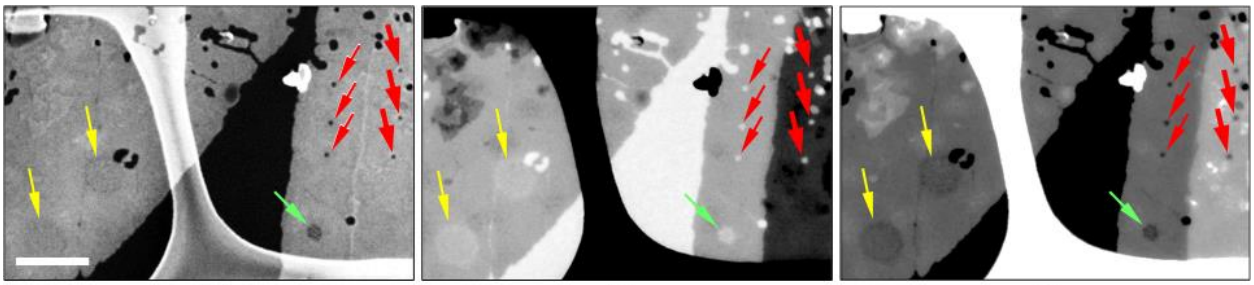

Figure 4. Images of zeolite nanosheet damage after using a 30 keV beam to probe the sample in several locations with different underfocus settings. (a) A secondary electron image with 200 nm scale bar. (b) Bright-field transmission image. (c) An annular dark-field transmission image. Colored inset arrows indicate beam positions where underfocus was set to 0.0 μm (WD = 13.78 mm, red), 20 μm (WD = 13.80 mm, green), and 50 μm (WD = 13.83 mm, yellow).

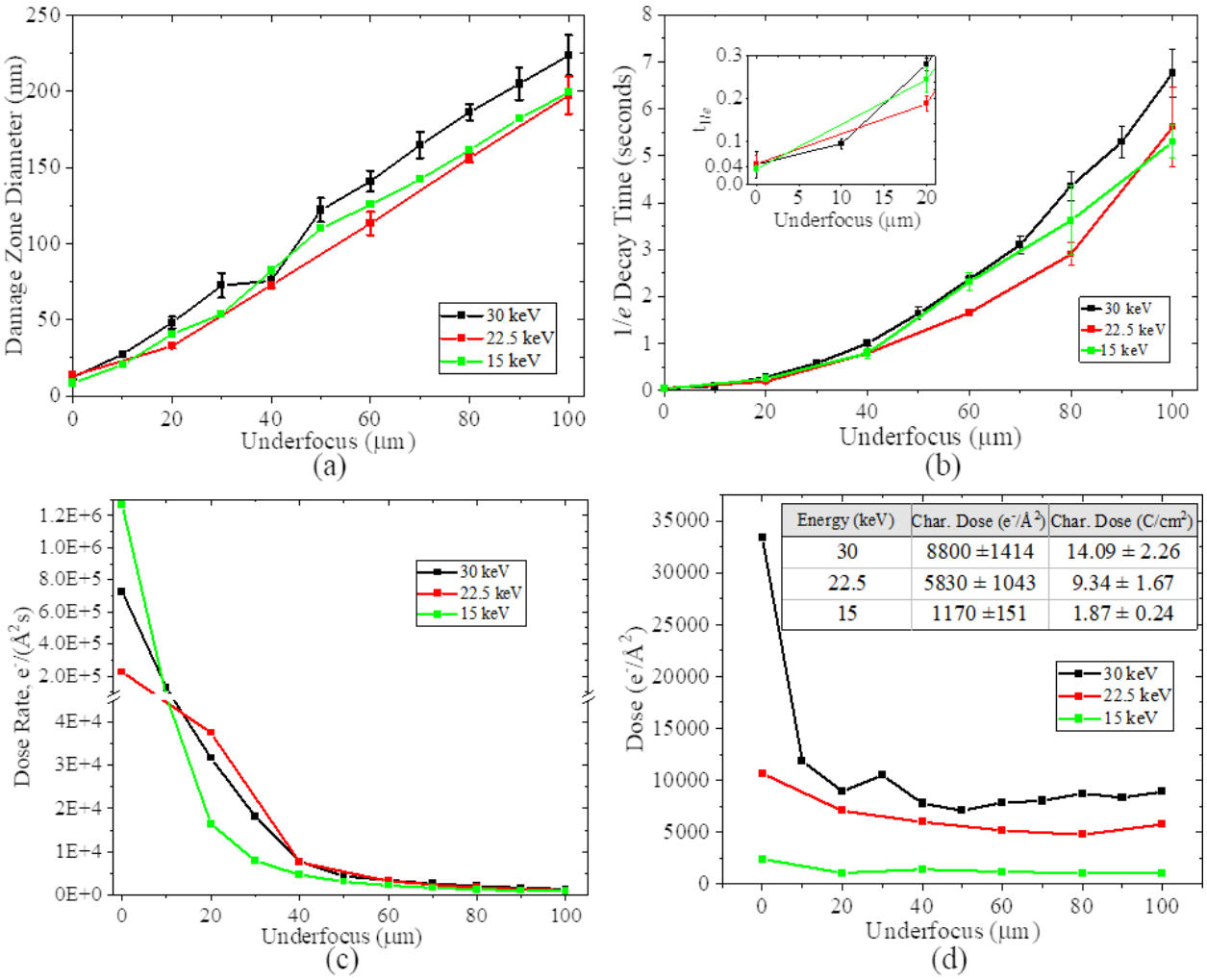

Figure 5. (a) The relationship between damage zone diameter and underfocus at different beam energies. (b) The $t_{1/e}$ intensity decay time for the background-subtracted (200) reflection as a function of beam energy. (c) Beam dose rate at different beam energies. (d) Beam dose at $t_{1/e}$ and different beam energies. The inset table shows the average characteristic dose in electrons/Å^2 and in C/cm^2 at the three beam energies.

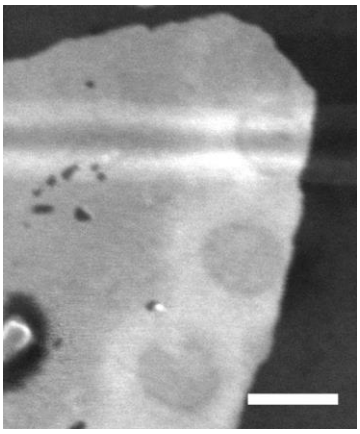

Figure 6. A 15 keV secondary electron image recorded with the InLens detector after exposing the sample to a stationary 15 keV electron beam (70 μm underfocus) at several locations adjacent to the edge of a zeolite nanosheet. The bright horizontal lines are a strong indication of sample charging.